

## FeF<sub>3</sub> as Reversible Cathode for All-Solid-State Fluoride Batteries

Inoishi, Atsushi

Institute for Materials Chemistry and Engineering, Kyushu University

Setoguchi, Naoko

Institute for Materials Chemistry and Engineering, Kyushu University

Hori, Hironobu

Institute for Materials Chemistry and Engineering, Kyushu University

Kobayashi, Eiichi

Kyushu Synchrotron Light Research Center

他

<https://hdl.handle.net/2324/7161289>

---

出版情報 : Advanced Energy and Sustainability Research. 3 (12), 2022-10-07. Wiley

バージョン :

権利関係 : Creative Commons Attribution 4.0 International



# FeF<sub>3</sub> as Reversible Cathode for All-Solid-State Fluoride Batteries

Atsushi Inoishi,\* Naoko Setoguchi, Hironobu Hori, Eiichi Kobayashi, Ryo Sakamoto, Hikari Sakaebe, and Shigeto Okada

Fluoride batteries are attracting intensive attention because they can provide a higher energy density than conventional lithium-ion batteries. Among various metal fluorides, FeF<sub>3</sub> is a promising candidate for the cathode material of fluoride batteries because of its high theoretical capacity. In this report, the reversibility of an FeF<sub>3</sub> cathode is investigated in conjunction with fluorite-type Ba<sub>0.6</sub>La<sub>0.4</sub>F<sub>2.4</sub> as the electrolyte and Pb as the counter-electrode material. For the first time, the discharge–charge performance of a fluoride battery using FeF<sub>3</sub> cathode is investigated. The initial discharge capacity is 579 mAh g<sup>−1</sup>, and a capacity of 461 mAh g<sup>−1</sup> is retained at the 10th cycle. The reversible conversion reaction mechanism for FeF<sub>3</sub> is clarified by X-ray diffraction and X-ray adsorption spectroscopy. The results revealed that FeF<sub>3</sub> is reduced to FeF<sub>2</sub> at the first-stage plateau and then to Fe metal at the second-stage plateau; they also reveal that the reverse process proceeded during charging. Ex situ scanning electron microscopy observations show that the morphology of the cathode changed reversibly and that, when the battery is in the discharged state, voids are present because of shrinkage of the electrode.

## 1. Introduction

Fluoride batteries have attracted significant attention because they demonstrate high specific energy densities and can accommodate flexible electrode materials. Fluoride (F<sup>−</sup>) anions function as charge carriers, meaning that numerous metals

can potentially be used as electrode materials in both the anode and cathode. In addition, numerous F<sup>−</sup>-ion conductors that exhibit high ionic conductivity have been reported.<sup>[1–22]</sup> Therefore, in addition to batteries that use a liquid electrolyte,<sup>[23–30]</sup> some all-solid-state fluoride-shuttle systems have been demonstrated.<sup>[12,31–43]</sup> As detailed in these previous reports, multivalent electrochemical reactions occur in such devices, and the devices can potentially deliver high energy densities via conversion-type reactions. Table S1, Supporting Information summarizes the theoretical energy density of some electrode materials. These values were calculated on the basis of the theoretical voltage and theoretical capacity. The theoretical capacity was calculated based on the change in the Gibbs free energy.

Among the possible cathode materials for fluoride-shuttle batteries, FeF<sub>3</sub> has the advantages of a large theoretical capacity (713 mAh g<sup>−1</sup>) and low cost. The theoretical gravimetric energy density for a full cell composed of an FeF<sub>3</sub> cathode and Mg anode is 1178 Wh kg<sup>−1</sup>, which is substantially higher than that obtainable from a standard Li<sup>+</sup>-ion battery. In the case of Li<sup>+</sup>-ion batteries, FeF<sub>3</sub> is considered one of the most promising conversion-type cathode materials.<sup>[41–46]</sup> In a Li<sup>+</sup>-ion battery with an FeF<sub>3</sub>-based cathode, the following reaction occurs and an insulator, LiF, is formed, which subsequently blocks the diffusion of Li<sup>+</sup> ions



However, in the case of the fluoride-shuttle system, the following simple reaction occurs without the formation of an insulator such as LiF




This lack of insulator formation is possibly an advantage of the fluoride-shuttle system compared with lithiation when FeF<sub>3</sub> is used as a cathode material. Although some fluoride batteries have been studied, FeF<sub>3</sub> has not been previously reported as a cathode material in a fluoride battery. In the present study, we report all-solid-state fluoride batteries based on FeF<sub>3</sub> as the cathode material.

A. Inoishi, N. Setoguchi, H. Hori, H. Sakaebe, S. Okada  
Institute for Materials Chemistry and Engineering  
Kyushu University  
Kasuga-Koen 6-1, Kasuga-shi, Fukuoka 816-8580, Japan  
E-mail: inoishi@cm.kyushu-u.ac.jp

E. Kobayashi  
Kyushu Synchrotron Light Research Center  
Yanagigaoka 8-7, Tosu-shi, Saga 841-0005, Japan

R. Sakamoto  
Office of Society Academia Collaboration for Innovation  
Kyoto University  
Funai Center, Nishikyo-ku, Kyoto 615-8530, Japan

 The ORCID identification number(s) for the author(s) of this article can be found under <https://doi.org/10.1002/aesr.202200131>.

© 2022 The Authors. Advanced Energy and Sustainability Research published by Wiley-VCH GmbH. This is an open access article under the terms of the Creative Commons Attribution License, which permits use, distribution and reproduction in any medium, provided the original work is properly cited.

DOI: 10.1002/aesr.202200131

## 2. Results and Discussion

### 2.1. XRD, XAS and SEM Evaluations of FeF<sub>3</sub> Cathode

Figure S1a,b, Supporting Information show scanning electron microscopy (SEM) images of the FeF<sub>3</sub> powder and Ba<sub>0.6</sub>La<sub>0.4</sub>F<sub>2.4</sub> (BLF, solid electrolyte) powder, respectively. The FeF<sub>3</sub> powder was used after being mechanically milled at a rotation rate of 600 rpm for 12 h. The FeF<sub>3</sub> particle size was uniform, and the size of the primary particles was  $\approx 100$  nm. The size of the secondary particles was  $\approx 500$  nm. By comparison, the BLF particle size was less uniform. Although the primary BLF particles were smaller than 1  $\mu\text{m}$ , secondary particles larger than 10  $\mu\text{m}$  were observed. In the present study, fluorite-type BLF was used as a solid electrolyte. BLF exhibits high F<sup>−</sup> ion conductivity with an interstitial-type transport mechanism.<sup>[21,22]</sup> Figure S2, Supporting Information shows the electrical conductivity of BLF prepared by mechanical milling. The electrical conductivity at 160 °C was  $3.8 \times 10^{-5} \text{ S cm}^{-1}$ . X-ray diffraction (XRD) patterns for the BLF electrolyte and FeF<sub>3</sub> composite electrode are shown in Figure 1a, together with the patterns for FeF<sub>3</sub>

and BaF<sub>2</sub>. FeF<sub>3</sub> powder was used after being mechanically milled. For the BLF electrolyte, only a single phase with a fluorite structure was observed, suggesting the formation of a solid solution. The peak positions were shifted because of the doping by La<sup>3+</sup>, which has a smaller radius than Ba<sup>2+</sup>. The broadened peaks in the pattern for the BLF electrolyte are due to the small crystallite size after mechanical milling. In the pattern for the composite electrode powder, only peaks corresponding to BLF and FeF<sub>3</sub> were observed, indicating that the composite powder was successively mixed without a significant side reaction.

Figure 1b shows an F K-edge X-ray absorption spectroscopy (XAS) spectrum of the FeF<sub>3</sub> composite electrode powder after ball milling. The XAS spectra of FeF<sub>3</sub> and BLF are also shown in this figure. The spectra of the composite electrode and pure FeF<sub>3</sub> show peaks at  $\approx 684$  eV. These peaks are assigned to the transition to mixed Fe3d–F2p unoccupied states in iron fluorides.<sup>[45,47]</sup> By contrast, the BLF does not absorb in this region, and its spectrum shows strong peaks between 686 and 693 eV. The spectrum of the electrode mixture shows peaks related to both FeF<sub>3</sub> and BLF. Figure 1c shows an Fe L-edge XAS spectrum of the FeF<sub>3</sub> composite electrode powder, along with the spectra of

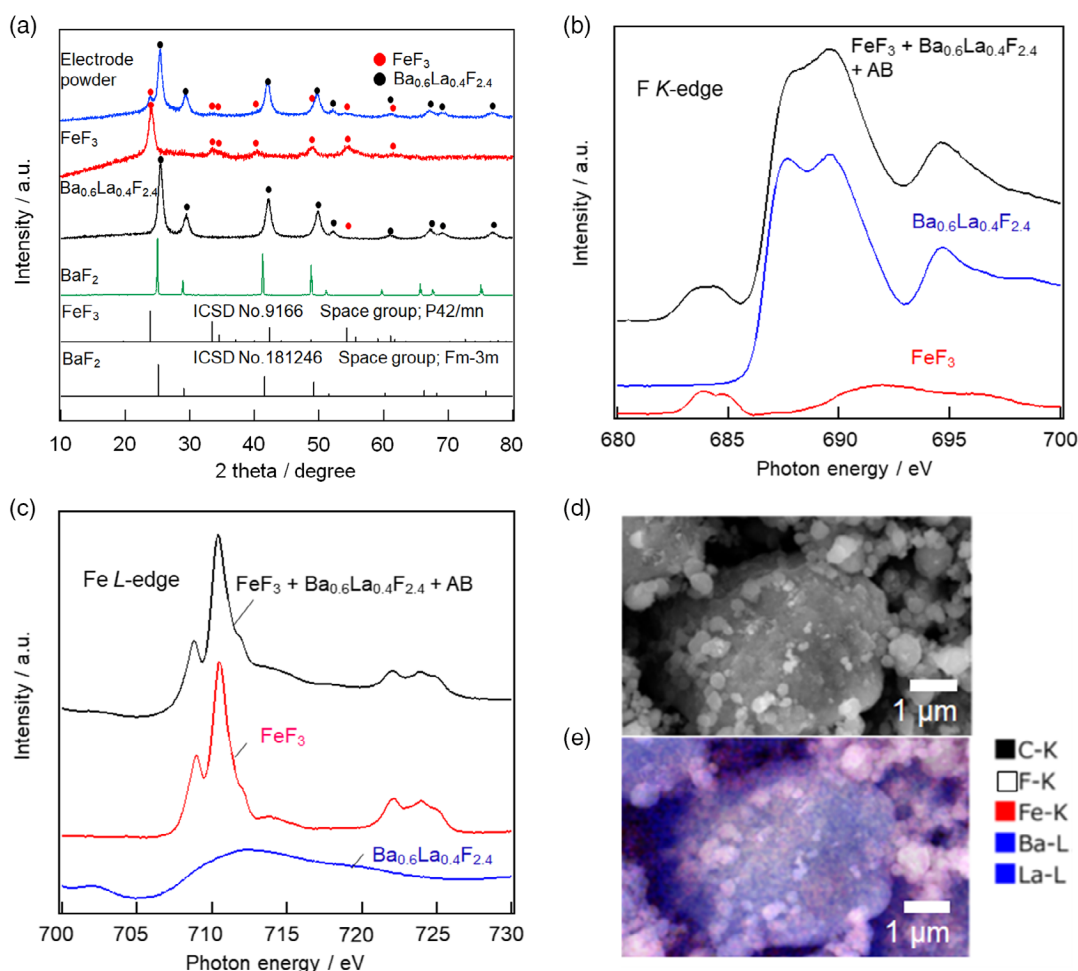


**Figure 1.** a) XRD patterns for FeF<sub>3</sub>, Ba<sub>0.6</sub>La<sub>0.4</sub>F<sub>2.4</sub>, and FeF<sub>3</sub> composite electrode powders. The pattern for BaF<sub>2</sub> is shown for reference. b) F K-edge XAS spectra and c) Fe L-edge XAS spectra of FeF<sub>3</sub> composite electrode powder. For comparison, XAS spectra of FeF<sub>3</sub> and BLF are also shown in these figures. d) SEM and e) EDS mapping images of FeF<sub>3</sub> composite electrode powder.

pure  $\text{FeF}_3$  and BLF. The strong peaks between 707 and 713 eV are approximately the same in the spectrum of the composite electrode and the pure  $\text{FeF}_3$ . These results indicate that  $\text{FeF}_3$  is chemically stable after being mixed with BLF and acetylene black (AB) by mechanical milling and that the iron remains in the  $\text{Fe}^{3+}$  state. Figure 1d,e show an field-emission SEM (FE-SEM) image and an energy dispersive X-ray spectrometry (EDS) mapping image of the  $\text{FeF}_3$  composite electrode, respectively. They show that the particle sizes in the BLF and  $\text{FeF}_3$  are  $\approx 5 \mu\text{m}$  and  $\approx 500 \text{ nm}$ , respectively. The BLF particle size is larger than that before compounding (Figure S1, Supporting Information).

In the present study, the electrochemical performance was evaluated at  $160^\circ\text{C}$  because of the resistance of the solid electrolyte. Therefore, we evaluated the stability of  $\text{FeF}_3$  at high temperatures. Figure S3, Supporting Information shows F *K*-edge and Fe *L*-edge XAS spectra of the  $\text{FeF}_3$  powder after it was heated at various temperatures. The spectra overlap within the investigated temperature range, indicating that  $\text{FeF}_3$  is stable to  $200^\circ\text{C}$ . The thermal stability of the composite electrode was also evaluated. Figure S4a, Supporting Information shows XRD patterns for a sample of the composite powder (BLF- $\text{FeF}_3$ -AB) after the sample was heated under an Ar atmosphere. At  $200^\circ\text{C}$ , no pattern changes were observed, in good agreement with the XAS measurement results in Figure S3, Supporting Information. At temperatures greater than  $250^\circ\text{C}$ , peaks due to  $\text{FeF}_2$  were newly observed, indicating that the  $\text{FeF}_3$  phase is stable in the composite powder to  $200^\circ\text{C}$  but decomposes at higher temperatures. XRD patterns for the pure  $\text{FeF}_3$  powder samples heated under an Ar atmosphere were also acquired (Figure S4b, Supporting Information). Peaks due to  $\text{Fe}_2\text{O}_3$  were newly observed in the pattern for the sample heated at  $400^\circ\text{C}$ . Therefore, the phase stability of  $\text{FeF}_3$  differed between the composite powder and the pure  $\text{FeF}_3$ .

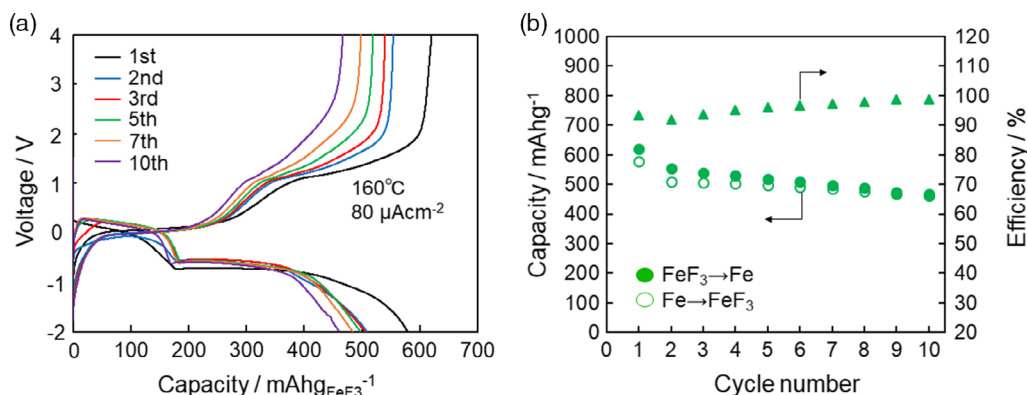
## 2.2. Electrochemical Performance of $\text{FeF}_3$ Cathode for the All-Solid-State Fluoride Battery

Figure 2a shows the discharge–charge profiles for the all-solid-state fluoride battery prepared using an  $\text{FeF}_3$  electrode. The cell had a  $\text{Pb}/\text{PbF}_2\text{--}\text{SnF}_2\text{--}\text{AB}/\text{BLF}/\text{FeF}_3\text{--}\text{BLF--}\text{AB}$  structure

as shown in Figure S5, Supporting Information. To evaluate the cathode performance of  $\text{FeF}_3$ , a bilayer-type counter electrode was used. The initial discharge capacity was  $579 \text{ mAh g}^{-1}$ . Therefore,  $2.4 \text{ F}^-$  ions were shuttled from the  $\text{FeF}_3$ . The observed capacity was 81% of the theoretical capacity of  $\text{FeF}_3$ . The observed capacity is substantially greater than that reported for a  $\text{CuF}_2$  electrode or a  $\text{BiF}_3$  electrode in an all-solid-state fluoride battery.<sup>[31,32,34]</sup> Thieu et al. reported that a  $\text{CuF}_2$  electrode delivered a capacity of  $360 \text{ mAh g}^{-1}$  in the first discharge, which is 68% of the theoretical capacity ( $527 \text{ mAh g}^{-1}$ ).<sup>[32]</sup> Therefore, both the capacity and utilization of our  $\text{FeF}_3$  electrode are superior to those for a  $\text{CuF}_2$  electrode. This result is speculatively attributed to the measurement temperature being slightly higher than that for the  $\text{CuF}_2$  case ( $150^\circ\text{C}$ ) and to the Pb-based negative electrode material exhibiting better fluorination characteristics than La. Bhatia et al. reported that a  $\text{BiF}_3$  electrode delivered a capacity of  $\approx 245 \text{ mAh g}^{-1}$  in the first discharge, which is 81% of the theoretical capacity ( $302 \text{ mAh g}^{-1}$ ).<sup>[34]</sup> Therefore, the utilization of  $\text{FeF}_3$  is similar to that of  $\text{BiF}_3$ .

Figure 2b shows the cycling characteristics of the all-solid-state fluoride-shuttle battery with an  $\text{FeF}_3$  electrode. Although some performance loss is apparent, the device was generally stable for 10 cycles. A discharge capacity of  $461 \text{ mAh g}^{-1}$  was retained at the 10th cycle. This cycling stability is also superior to that of a  $\text{BiF}_3$  electrode or a  $\text{CuF}_2$  electrode in all-solid-state fluoride batteries.<sup>[31,32,34]</sup> The overpotential in the second plateau of the discharge profile for a  $\text{FeF}_3$  cathode in a lithium-conversion-type battery has been reported to be larger than that in the first plateau.<sup>[44]</sup> However, according to the results for the fluoride battery in the present work, the polarization was smaller in the lower potential plateau. In addition, although the temperature conditions differed, the voltage difference between charging and discharging in the second plateau was smaller in the fluoride shuttle battery than in the lithium-ion battery. This result suggests that the resistance differs depending on the discharge–charge mechanism for lithium-conversion-type and fluoride-shuttle-type batteries.

Figure S6, Supporting Information shows discharge–charge profiles at various current densities. With increasing current density, both the discharge and charge capacity decreased. When the current density was  $0.24$  and  $0.16 \text{ mA cm}^{-2}$ , the initial discharge capacity was  $309$  and  $510 \text{ mAh g}^{-1}$ , respectively.



**Figure 2.** a) Discharge–charge profiles for all-solid-state fluoride battery with  $\text{FeF}_3$  electrode. b) Cycle properties of all-solid-state fluoride battery with  $\text{FeF}_3$  electrode.

At  $0.24 \text{ mA cm}^{-2}$ , the IR drop associated with the BLF electrolyte was calculated to be  $\approx 500 \text{ mV}$  from the ionic conductivity of BLF (Figure S2, Supporting Information). The difference in cell voltage between discharging and charging was  $\approx 1 \text{ V}$  at the second plateau, which is at a lower potential. Therefore, a large part of the resistance is related to the IR drop in the BLF solid electrolyte layer. Consequently, the resistance of the battery would be substantially decreased with the incorporation of a solid electrolyte with high  $\text{F}^-$  ion conductivity.

### 2.3. Discharge-Charge Mechanism of the $\text{FeF}_3$ Cathode for the All-Solid-State Fluoride Battery

To clarify the discharge-charge mechanism for the  $\text{FeF}_3$  cathode, we conducted ex situ XRD and XAS measurements. The measurement points are indicated in Figure S7, Supporting Information. Figure 3 shows ex situ XRD patterns before and after the discharge-charge measurements. At the initial state, only peaks due to BLF and  $\text{FeF}_3$  were observed. After discharge to  $350 \text{ mAh g}^{-1}$ , peaks associated with  $\text{FeF}_2$  were present. After discharge to  $-2 \text{ V}$ , a peak due to Fe metal was newly observed. After charging to  $300 \text{ mAh g}^{-1}$ , this peak disappeared and the intensity of the peaks assigned to  $\text{FeF}_2$  increased. Moreover, the intensity of these peaks decreased after charging to  $4 \text{ V}$ . These results indicate that the following reactions occur in the  $\text{FeF}_3$  electrode

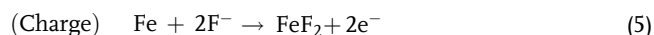
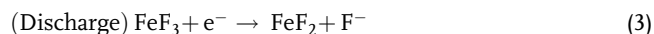
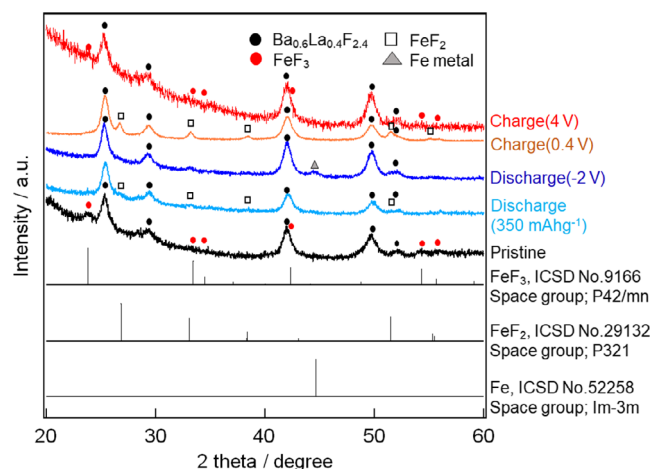


Figure 4a shows ex situ F K-edge XAS spectra of the  $\text{FeF}_3$  electrode before and after the discharge-charge measurement. Before the electrochemical measurement, adsorption by  $\text{FeF}_3$  was observed at  $684 \text{ eV}$  (Figure 1b). The intensity of this peak gradually decreased as discharging progressed and then



**Figure 3.** Ex situ XRD patterns before and after discharge-charge measurements.

increased as charging progressed. However, the adsorption peaks between  $686$  and  $693 \text{ eV}$  are mainly due to the BLF, with a small contribution from  $\text{FeF}_3$ . The shape of the spectrum corresponding to the discharged state agrees well with that for BLF because of defluorination of  $\text{FeF}_3$ .

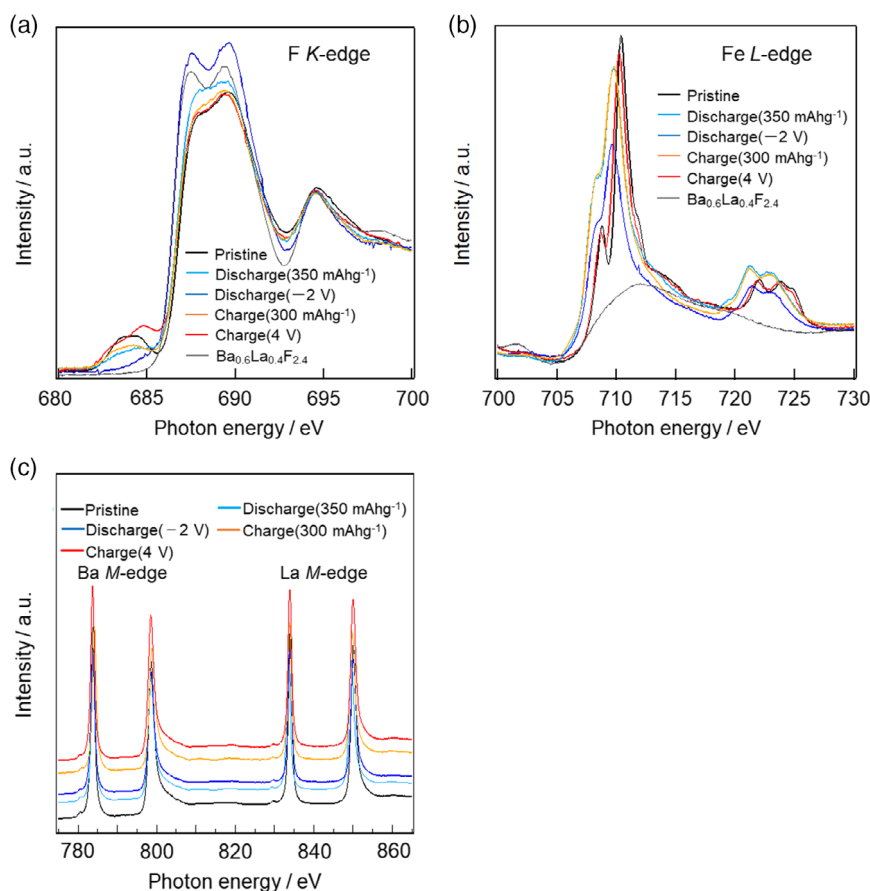
Figure 4b shows ex situ Fe L-edge XAS spectra of the  $\text{FeF}_3$  electrode before and after the discharge-charge measurement. The spectra show two intense peaks at the  $L_3$ -edge (between  $705$  and  $715 \text{ eV}$ ) and two doublet peaks at the  $L_2$ -edge (between  $718$  and  $726 \text{ eV}$ ). The positions of these peaks shifted to lower energy as discharging progressed and returned to almost their original positions upon charging. As already shown in Figure 1c, the peak positions in the Fe L-edge spectrum of the  $\text{FeF}_3$  composite powder are the same as those in the spectrum of pure  $\text{FeF}_3$ , suggesting that the valence number at the initial state is  $\text{Fe}^{3+}$  (i.e.,  $\text{FeF}_3$ ). Miedema et al. reported that the peak position for  $\text{FeF}_3$  in the  $L_3$ -edge spectrum is higher than that for  $\text{FeF}_2$ .<sup>[48]</sup> Senoh et al. reported the peak position for  $\text{FeF}_2$  in the L-edge spectrum is higher than that for  $\text{Fe}$ .<sup>[45]</sup> These results indicate that  $\text{Fe}^{3+}$ ,  $\text{Fe}^{2+}$ , and Fe metal can be distinguished by their peak positions. The shapes of the reported spectra are similar to those of the spectra after discharging to  $-2 \text{ V}$  and  $350 \text{ mAh g}^{-1}$ . The energy positions of the  $L_3$  peaks for Fe are lower than those for  $\text{FeF}_2$ , and the intensity of the Fe peaks is diminished. These results suggest that redox reactions of  $\text{Fe}^{3+}/\text{Fe}^{2+}$  and  $\text{Fe}^{2+}/\text{Fe}$  occur during the discharge-charge reaction. This result is in good agreement with the XRD results shown in Figure 3.

Figure 4c present ex situ Ba L-edge and La M-edge XAS spectra of the  $\text{FeF}_3$  electrode before and after the discharge-charge measurements. The peak positions in both spectra were the same before and after the measurements, suggesting that the BLF electrolyte is electrochemically stable and that the redox couple is  $\text{Fe}^{3+}/\text{Fe}$ .

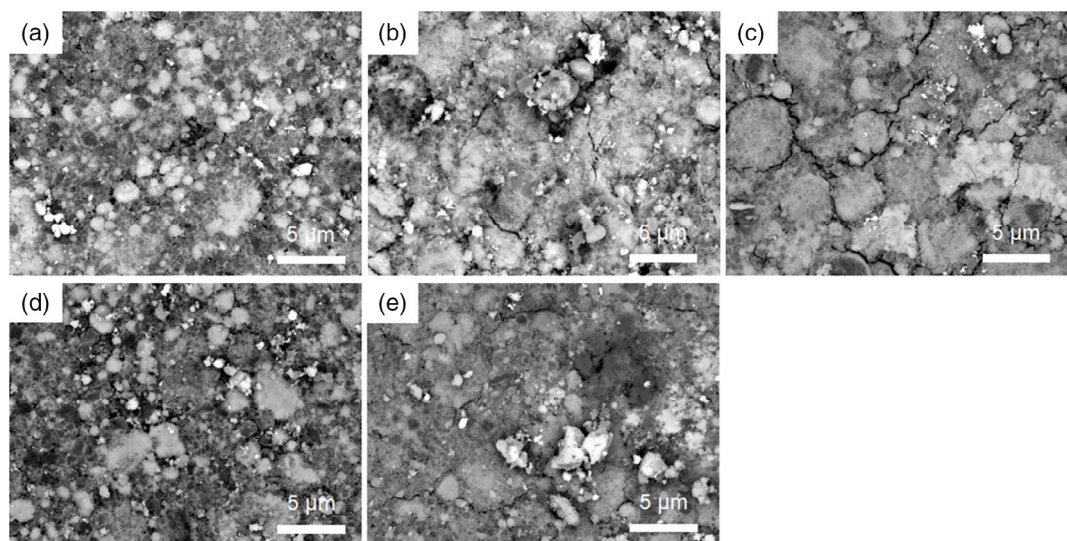
When a conversion-type reaction occurs in the  $\text{FeF}_3$  electrode, the resultant volume change is larger than that associated with a typical insertion-type reaction. Theoretically, the volume change is  $\approx 75\%$  according to Equation (2). Therefore, we assumed that degradation is mainly caused by the breaking of ionic or electronic connections as a result of the large volume change. We examined the morphology of the  $\text{FeF}_3$  electrode before and after the discharge-charge measurements. Figure S8a, Supporting Information shows EDS mapping images of the  $\text{FeF}_3$  electrode before the discharge-charge measurements. The battery cell was constructed and heated at  $160^\circ\text{C}$  for  $2 \text{ h}$ ; the electrode was then removed from the cell without electrochemical treatment. Carbon was found to be uniformly dispersed, and the positions of Fe and La were clearly separated, indicating that  $\text{FeF}_3$  and BLF were mixed without significant solid solution formation. The bright regions of the images correspond to La, which is a heavy element, and the BLF and  $\text{FeF}_3$  components can be clearly distinguished from the light and dark regions in the SEM images. In addition, after the initial discharge (Figure S8b, Supporting Information), the bright regions correspond to La and the dark regions correspond mainly to Fe.

Figure 5a–e shows SEM images (magnification:  $5000\times$ ) with different cutoff conditions for the discharge-charge measurements. The bright area indicates the presence of heavy elements such as Ba and La. In the discharged state (Figure 5c), a large





**Figure 4.** Ex situ a) F K-edge, b) Fe L-edge, and c) Ba M-edge and La M-edge XAS spectra of  $\text{FeF}_3$  electrode before and after discharge–charge measurements.



**Figure 5.** SEM images of  $\text{FeF}_3$  electrode before and after discharge–charge measurements (magnification: 5000 $\times$ ). a) Before discharge–charge measurement. The battery cell was constructed and heated at 433 K for 2 h, the cell was then cooled to room temperature, and the electrode was collected. b) After discharging to 350  $\text{mAh g}^{-1}$ . c) After discharging to  $-2$  V (endpoint of discharge). d) After charging to 300  $\text{mAh g}^{-1}$ . e) After discharging to 4 V (endpoint of charge).

proportion of bright areas is observed. This is reasonable given that the volume of iron fluoride is decreased after discharge because the iron is reduced to Fe metal. On the other hand, the number of cracks increased as discharging progressed and decreased as charging progressed. Figure S9a–e, Supporting Information show SEM images (magnification: 50 000 $\times$ ) with different cutoff conditions for discharge–charge measurements. At the initial state, FeF<sub>3</sub> (dark regions) with a thickness of 100–500 nm is coated with a thin BLF layer ( $\approx$ 70 nm). After discharge to  $-2$  V, FeF<sub>3</sub> is still coated with a thin BLF layer, although voids are evident. A similar morphology was observed between the initial state (Figure S9a, Supporting Information) and the cell after charging to 4 V (Figure S9e, Supporting Information). These results indicate that no significant size change of the iron fluoride occurred before and after the initial cycle.

A better cyclability may be performed if the potential window would set to only cycle the battery between FeF<sub>3</sub> and FeF<sub>2</sub>. Discharge–charge profiles for the conversion-type FeF<sub>3</sub> cathode of the lithium battery has been reported, and it showed that a better energy efficiency was observed with only one lithium insertion.<sup>[49]</sup> Therefore, the effect of the conditions of the cut off voltage will be reported in our future work to investigate the degradation mechanism.

### 3. Conclusion

In summary, the electrochemical reversibility of FeF<sub>3</sub> has been demonstrated in an all-solid-state fluoride battery for the first time. The FeF<sub>3</sub> electrode exhibits a reversible capacity of 579 mAh g<sup>-1</sup> at the initial cycle and retains a discharge capacity of 461 mAh g<sup>-1</sup> at the 10th cycle. The XRD and XAS results suggest that the FeF<sub>3</sub> is first reduced to FeF<sub>2</sub> during discharging, and then to Fe. The reverse reaction occurs during charging. SEM imaging reveals that the number of cracks increases as discharging progresses and decreases as charging progresses and the volume of FeF<sub>3</sub> electrode changes. The results presented here indicate that FeF<sub>3</sub> is a promising electrode material for fluoride batteries with a large energy storage capacity.

### 4. Experimental Section

**Battery Assembly:** BaF<sub>2</sub> (99.9%) was purchased from FUJIFILM Wako Pure Chemical. LaF<sub>3</sub> (99.95%) was purchased from Kishida Chemical. FeF<sub>3</sub> (99%) was purchased from Strem Chemicals. Pb (99.95%), PbF<sub>2</sub> (99%), and SnF<sub>2</sub> (99%) were purchased from Sigma-Aldrich. Acetylene black (AB) was purchased from Denka. Mechanical milling was used to synthesize Ba<sub>0.6</sub>La<sub>0.4</sub>F<sub>2.4</sub> (BLF) from a stoichiometric mixture of BaF<sub>2</sub> and LaF<sub>3</sub>; milling was conducted at a rotation rate of 600 rpm for 12 h under Ar. The ball-to-powder mass ratio was kept constant at 20:1 during this synthesis process, and ZrO<sub>2</sub> pots (80 mL volume) and 36 g spheres (3 mm diameter) were used as milling media. Mechanical milling was performed using a planetary-type mill (TRITSCH Pulverisette 7). BLF was used as the electrolyte, and the cathode was prepared by mixing FeF<sub>3</sub>, BLF, and AB (FeF<sub>3</sub>–BLF–AB) in a 6:10:1 weight ratio. The counter electrode contained two layers: a Pb layer and a PbF<sub>2</sub>–SnF<sub>2</sub>–AB composite layer. The Pb layer was prepared by compacting Pb powder. A PbF<sub>2</sub>–SnF<sub>2</sub>–AB composite layer was prepared by pressing a composite powder containing PbF<sub>2</sub>, SnF<sub>2</sub>, and AB; this powder was prepared by mechanically milling a mixture of PbF<sub>2</sub>, SnF<sub>2</sub>, and AB combined in a 3:1.4:0.286 weight ratio. First, PbF<sub>2</sub> and SnF<sub>2</sub> and 10 ZrO<sub>2</sub> balls (10 mm diameter) were mixed at a

rotation rate of 600 rpm for 24 h under Ar. AB was then added to the obtained powder composed of PbF<sub>2</sub> and SnF<sub>2</sub>, and the resultant mixture was mixed at a rotation rate of 600 rpm for 12 h under Ar.

**Electrochemical Procedure and Analyses:** Impedance measurements were conducted using a potentiostat/galvanostat (Bio-Logic SP-300) over the frequency range from 7 MHz to 0.1 Hz, with the sample under an Ar atmosphere. The specimens were prepared as 10 mm-diameter,  $\approx$ 0.6-mm-thick pellets via uniaxial cold-pressing under a force of 510 MPa. A thin Pt layer was sputtered onto both sides of each pellet to form ion-blocking electrodes. The resultant pellets were sealed in a HS cell (Hohsen) in an Ar-filled glove box. Each all-solid-state fluoride-shuttle cell was assembled using an insulating cell die (PEEK, poly ether ether ketone) sandwiched between two stainless steel rods. The cell was assembled under Ar by pressing the cathode, electrolyte, and counter electrode materials together under an applied force of 510 MPa to obtain a 10 mm-diameter disc. A four-layer cell (Pb layer, 380  $\mu$ m/PbF<sub>2</sub>–SnF<sub>2</sub>–AB layer, 370  $\mu$ m/Ba<sub>0.6</sub>La<sub>0.4</sub>F<sub>2.4</sub> layer, 800  $\mu$ m/FeF<sub>3</sub>–BLF–AB layer, 180  $\mu$ m) was thus obtained. In the present study, a thick FeF<sub>3</sub> layer (180  $\mu$ m) was used for evaluation of the electrochemical performance. Electrochemical charge–discharge measurements were performed in galvanostatic mode using a discharge–charge cycling apparatus (HJ1020mSD8, Hokuto Denko). Each cell was cycled at 160  $^{\circ}$ C at a different current density (0.08, 0.16, or 0.24 mA cm<sup>-2</sup>) in the voltage range  $-2$  to 4 V. XRD patterns of the powder samples and battery pellets were recorded using a Rigaku Miniflex and a Rigaku RINT-TTRIII equipped with a parallel beam. The surface morphology of the pellets was investigated by field-emission SEM (FE-SEM) using a JEOL JSM-IT700HR/LA. XAS data using soft X-rays were acquired at the BL-12 beamline station of the SAGA Light Source. All experiments were performed without exposure to the air, except during SEM observations.

### Supporting Information

Supporting Information is available from the Wiley Online Library or from the author.

### Acknowledgements

This paper is based on results obtained from the projects, JPNP16001 and JPNP21006, commissioned by the New Energy and Industrial Technology Development Organization (NEDO). The experiments using synchrotron radiation were performed at beamline BL12 of the SAGA Light Source (Proposal No. 2201156F).

### Conflict of Interest

The authors declare no conflict of interest.

### Data Availability Statement

The data that support the findings of this study are available from the corresponding author upon reasonable request.

### Keywords

all-solid-state batteries, fluoride batteries, iron fluoride

Received: September 1, 2022

Revised: September 27, 2022

Published online: October 7, 2022

- [1] R. Kanno, S. Nakamura, K. Ohno, Y. Kawamoto, *Mater. Res. Bull.* **1991**, 26, 1111.
- [2] S. Vilminot, G. Perez, W. Granier, L. Cot, *Solid State Ionics* **1981**, 2, 91.
- [3] Y. Ito, T. Mukoyama, S. Yoshikado, *Solid State Ionics* **1995**, 80, 317.
- [4] L. Liu, L. Yang, M. Liu, X. Li, D. Shao, K. Luo, X. Wang, Z. Luo, *J. Alloy. Compd.* **2020**, 819, 152983.
- [5] F. P. Pflügl, V. Epp, S. Nakhal, M. Lerch, M. Wilkening, *Phys. Status. Solidi C* **2015**, 12, 10.
- [6] L. Xiong, P. Wen, Y. Zhang, X. Liu, J. Ning, X. Wang, H. Wang, Z. Yang, *J. Power Sources* **2022**, 518, 230718.
- [7] I. Mohammad, R. Witter, M. Fichtner, M. A. Reddy, *ACS Appl. Energy Mater.* **2018**, 1, 4766.
- [8] L. Liu, L. Yang, D. Shao, K. Luo, C. Zou, Z. Luo, X. Wang, *Ceram. Int.* **2020**, 46, 20521.
- [9] A. Düvel, S. Wegner, K. Efimov, A. Feldhoff, P. Heitjans, M. Wilkening, *J. Mater. Chem.* **2011**, 21, 6238.
- [10] A. Düvel, M. Wilkening, S. Wegner, A. Feldhoff, V. Šepelák, P. Heitjans, *Solid State Ionics* **2011**, 184, 65.
- [11] A. Düvel, M. Wilkening, R. Uecker, S. Wegner, V. Šepelák, P. Heitjans, *Phys. Chem. Chem. Phys.* **2010**, 10, 11251.
- [12] I. Mohammad, J. Chable, R. Witter, M. Fichtner, M. A. Reddy, *ACS Appl. Mater. Interfaces* **2018**, 10, 17249.
- [13] S. Breuer, M. Wilkening, *Dalton Trans.* **2018**, 47, 4105.
- [14] L. Zhang, M. A. Reddy, P. Gao, M. Fichtner, *J. Alloy. Compd.* **2016**, 684, 733.
- [15] L. Zhang, M. A. Reddy, M. Fichtner, *Solid State Ionics* **2015**, 272, 39.
- [16] S. Breuer, S. Lunghammer, A. Kiesl, M. Wilkening, *J. Mater. Sci.* **2018**, 53, 13669.
- [17] J. Chable, B. Dieudonné, M. Body, C. Legein, M. P. Crosnier-Lopez, C. Galven, F. Mauvy, E. Durand, S. Fourcade, D. Sheptyakov, M. Leblanc, V. Maisonneuve, A. Demourgues, *Dalton Trans.* **2015**, 44, 19625.
- [18] C. Rongeat, M. A. Reddy, R. Witter, M. Fichtner, *ACS Appl. Mater. Interfaces* **2014**, 6, 2103.
- [19] B. Dieudonné, J. Chable, F. Mauvy, S. Fourcade, E. Durand, E. Lebraud, M. Leblanc, C. Legein, M. Body, V. Maisonneuve, A. Demourgues, *J. Phys. Chem. C* **2015**, 119, 25170.
- [20] B. Dieudonné, J. Chable, M. Body, C. Legein, E. Durand, F. Mauvy, S. Fourcade, M. Leblanc, V. Maisonneuve, A. Demourgues, *Dalton Trans.* **2017**, 46, 3761.
- [21] A. Düvel, J. Bednarcik, V. Šepelák, P. Heitjans, *J. Phys. Chem. C* **2014**, 118, 7117.
- [22] C. Rongeat, M. A. Reddy, R. Witter, M. Fichtner, *J. Phys. Chem. C* **2013**, 117, 4943.
- [23] K. Okazaki, Y. Uchimoto, T. Abe, Z. Ogumi, *ACS Energy Lett.* **2017**, 2, 1460.
- [24] H. Konishi, T. Minato, T. Abe, Z. Ogumi, *J. Electrochem. Soc.* **2017**, 164, A3702.
- [25] X. Zhao, Z. Zhao-Karger, M. Fichtner, X. Shen, *Angew. Chem. Int. Ed.* **2020**, 59, 5902.
- [26] S. Kawachi, H. Nakamoto, R. Takekawa, T. Kobayashi, T. Abe, *ACS Appl. Energy Mater.* **2022**, 5, 2096.
- [27] X. Li, Y. Tang, J. Zhu, H. Lv, Y. Xu, W. Wang, C. Zhi, H. Li, *Adv. Energy Mater.* **2021**, 11, 2003714.
- [28] K. Shimoda, T. Minato, H. Konishi, G. Kano, T. Nakatani, S. Fujinami, A. C. Kucuk, S. Kawaguchi, Z. Ogumi, T. Abe, *J. Electroanal. Chem.* **2021**, 895, 115508.
- [29] M. Kawasaki, K. Morigaki, G. Kano, H. Nakamoto, R. Takekawa, J. Kawamura, T. Minato, T. Abe, Z. Ogumi, *J. Electrochem. Soc.* **2021**, 168, 010529.
- [30] T. Yamanaka, Z. Ogumi, T. Abe, *J. Mater. Chem. A* **2021**, 9, 22544.
- [31] M. A. Reddy, M. Fichtner, *J. Mater. Chem.* **2011**, 21, 17059.
- [32] D. T. Thieu, M. H. Fawey, H. Bhatia, T. Diemant, V. S. Chakravadhanula, R. J. Behm, C. Kübel, M. Fichtner, *Adv. Funct. Mater.* **2017**, 27, 1701051.
- [33] C. Rongeat, M. A. Reddy, T. Diemant, R. J. Behm, M. Fichtner, *J. Mater. Chem. A* **2014**, 2, 20861.
- [34] H. Bhatia, D. T. Thieu, A. H. Pohl, V. S. K. Chakravadhanula, M. H. Fawey, C. Kübel, M. Fichtner, *ACS Appl. Mater. Interfaces* **2017**, 9, 23707.
- [35] M. H. Fawey, V. S. K. Chakravadhanula, A. R. Munnangi, C. Rongeat, H. Hahn, M. Fichtner, C. Kübel, *J. Power Sources* **2020**, 466, 228283.
- [36] O. Clemens, C. Rongeat, M. A. Reddy, A. Giehr, M. Fichtner, H. Hahn, *Dalton Trans.* **2014**, 43, 15771.
- [37] D. Zhang, K. Yamamoto, Y. Wang, S. Gao, T. Uchiyama, T. Watanabe, T. Takami, T. Matsunaga, K. Nakanishi, H. Miki, H. Iba, K. Ameszawa, K. Maeda, H. Kageyama, Y. Uchimoto, *Adv. Energy Mater.* **2021**, 11, 2102285.
- [38] T. Tojigamori, H. Nakajima, H. Miki, N. Matsui, T. Nakatani, S. Fujinami, K. Noi, H. Tsukasaki, K. Suzuki, M. Hirayama, S. Mori, T. Abe, R. Kanno, *ACS Appl. Energy Mater.* **2022**, 5, 1002.
- [39] K. Nakayama, R. Ishikawa, T. Tojigamori, H. Miki, H. Iba, N. Shibata, Y. Ikuhara, *J. Mater. Chem. A* **2022**, 10, 3743.
- [40] A. Celik-Kucuk, T. Abe, *J. Power Sources* **2021**, 496, 229828.
- [41] F. Badway, F. Cosandey, N. Pereira, G. G. Amatucci, *J. Electrochem. Soc.* **2003**, 150, A1318.
- [42] W. Fu, E. Zhao, Z. Sun, X. Ren, A. Magasinski, G. Yushin, *Adv. Funct. Mater.* **2018**, 28, 1801711.
- [43] L. Li, R. Jacobs, P. Gao, L. Gan, F. Wang, D. Morgan, S. Jin, *J. Am. Chem. Soc.* **2016**, 138, 2838.
- [44] A. Kitajou, I. Tanaka, Y. Tanaka, E. Kobayashi, H. Setoyama, T. Okajima, S. Okada, *Electrochemistry* **2017**, 85, 472.
- [45] H. Senoh, K. Matsui, M. Shikano, T. Okumura, H. Kikuchi, K. Shimoda, K. Yamanaka, T. Ohta, T. Fukunaga, H. Sakaebe, E. Matsubara, *ACS Appl. Mater. Interfaces* **2019**, 11, 30959.
- [46] K. Yoshii, N. Taguchi, T. Miyazaki, M. Shikano, H. Sakaebe, *Chem. Commun.* **2020**, 56, 4878.
- [47] S. A. Krasnikov, A. S. Vinogradov, A. B. Preobrajenski, L. K. Gridneva, S. L. Molodtsov, C. Laubschat, R. Szargan, *Phys. Scr.* **2005**, T115, 1074.
- [48] P. S. Miedema, F. M. F. de Groot, *J. Electron Spectrosc.* **2013**, 187, 32.
- [49] M. Zhou, L. Zhao, A. Kitajou, S. Okada, J. Yamaki, *J. Power Sources* **2012**, 203, 103.